PHYSICAL REVIEW B **95**, 165203 (2017)

Electronic band structure of epitaxial PbTe (111) thin films observed by angle-resolved photoemission spectroscopy

Zhenyu Ye,[1] Shengtao Cui,[2] Tianyu Shu,[1] Songsong Ma,[1] Yang Liu,[1] Zhe Sun,[3] Jun-Wei Luo,[4] and Huizhen Wu[1,*]
[1]*Department of Physics, State Key Laboratory for Silicon Materials, Zhejiang University, Hangzhou 310027, China*
[2]*School of Physical Science and Technology, ShanghaiTech University and CAS-Shanghai Science Research Center, Shanghai 201203, China*
[3]*National Synchrotron Radiation Laboratory, University of Science and Technology of China, Hefei 230029, China*
[4]*State Key Laboratory of Superlattices and Microstructures, Institute of Semiconductors, Chinese Academy of Sciences, P. O. Box 912, Beijing 100083, China*

(Received 21 November 2016; revised manuscript received 28 March 2017; published 24 April 2017)

Using angle-resolved photoemission spectroscopy (ARPES), we studied bulk and surface electronic band structures of narrow-gap semiconductor lead telluride (PbTe) thin films grown by molecular beam epitaxy both perpendicular and parallel to the Γ-L direction. The comparison of ARPES data with the first-principles calculation reveals the details of band structures, orbital characters, spin-orbit splitting energies, and surface states. The photon-energy-dependent spectra show the bulk character. Both the L and Σ valence bands are observed and their energy difference is determined. The spin-orbit splitting energies at L and Γ points are 0.62 eV and 0.88 eV, respectively. The surface states below and close to the valence band maximum are identified. The valence bands are composed of a mixture of Pb 6s and Te 5 p_z orbitals with dominant in-plane even parity, which is attributed to the layered distortion in the vicinity of the PbTe (111) surface. These findings provide insights into PbTe fundamental properties and shall benefit relevant thermoelectric and optoelectronic applications.

DOI: 10.1103/PhysRevB.95.165203

I. INTRODUCTION

Narrow-gap lead telluride (PbTe) has attracted tremendous interest because of its unique properties and important applications. It has been widely used in thermoelectric and midinfrared optoelectronic devices [1,2], such as thermoelectric power generation with the highest efficiency at high temperature [3,4], infrared detectors [5], light-emitting diodes [6], and lasers [7]. Particularly, significant progress has been made in the past decades to improve the thermoelectric figure of merit of PbTe-based thermoelectric devices, including the application of Tl doping [3], band convergence engineering [8], and multiscale hierarchical design [4]. PbTe also hosts fascinating physical properties. Recently, Hsieh *et al.* theoretically predicted that PbTe could become a topological crystalline insulator by applying pressure, strain, or forming an alloy with SnTe [9]. A two-dimensional electron gas (2DEG) with high mobility has been discovered by Zhang *et al.* at the interface of rock-salt PbTe and II-VI zinc-blende CdTe, and the quantum oscillation measurements demonstrated the Dirac fermion nature of the 2DEG [10].

The band structures of PbTe are pivotal to the understanding of its outstanding performances. There have been a plethora of theoretical studies of energy-band structure of PbTe. The calculations of electronic band structure of PbTe have been carried out by using $\mathbf{k}\cdot\mathbf{p}$ perturbation theory [11], the empirical pseudopotential method [12], tight binding model [13], and first-principles calculations involving hybrid functional [14] and quasiparticle GW approximations [15]. For the experimental studies of the electronic band structure of PbTe, however, only band gaps at some specific k points were deduced from the optical reflectivity [16] and electroreflectivity [17] measurements. These measured results were interpreted in terms of Van Hove's singularities from transitions between bands at high-symmetry points and lines, without explicit momentum resolution in the entire Brillouin zone (BZ). Grandke *et al.* [18] performed measurements on the (100) surface of single crystals of lead chalcogenides using rare-gas resonance lines at 16.85 eV and 21.22 eV, which was one of the first angle-resolved photoemission spectroscopy (ARPES) studies of the semiconductor surfaces. They claimed that the indirect-transition model could be applied in lead chalcogenides with O_h symmetry due to a larger number of critical points along Γ-X of the BZ, whereas the direct-transition model is more applicable for Ge and zinc-blende semiconductors [18,19]. Hinkel *et al.* [20] also performed photoemission spectroscopy (PES) measurements using synchrotron radiation on the (100) surface of PbTe bulk crystal. The electron emission normal to the surface was recorded and the dispersions along Γ-X were obtained, and the direct-transition model was adopted to interpret the data. Though the (100) surface has been well studied, there is no systematic study regarding the (111) surface to our best knowledge. This is because the (111) surface is a strong polar surface and is difficult to cleavage from bulk single crystal, contrary to the (100) surface which is the natural cleavage plane for rock-salt single crystal. The band-edge states of PbTe which occur at the L point (direct band gap) is the most important for optical and transport properties of PbTe. To perform ARPES measurements around the L point, the (111) surface is the most suitable. The challenge can be resolved by performing ARPES characterizations of the PbTe (111) thin films grown by molecular beam epitaxy (MBE).

On the other hand, the band-inverted SnTe and its alloy with PbTe have been considered to be the prototype material of topological crystalline insulators [21,22]. The study of the normal narrow-gap PbTe might provide valuable information

---

[*] hzwu@zju.edu.cn

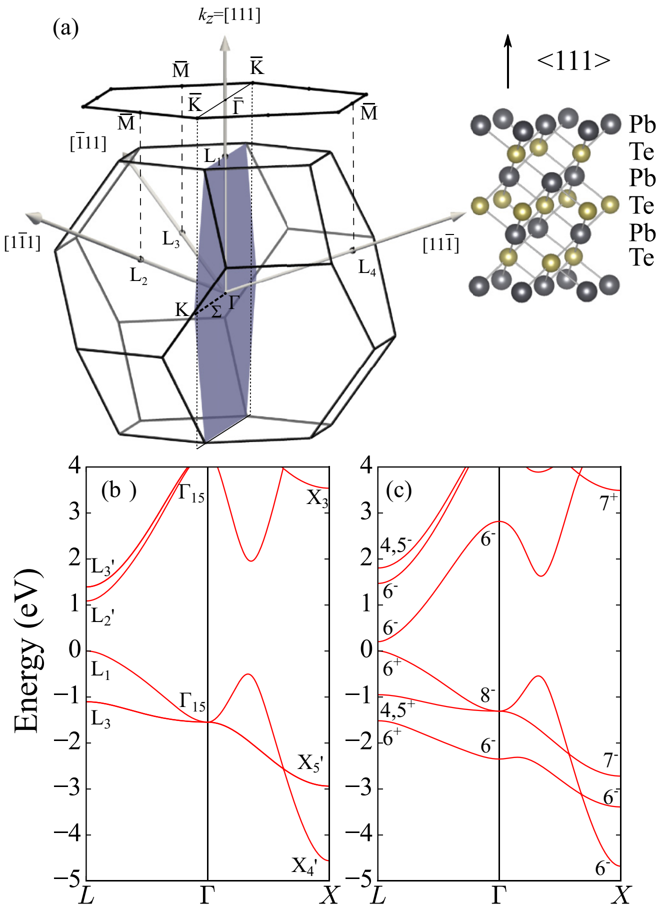

FIG. 1. (a) Bulk fcc BZ and the surface BZ. Inset: Lattice structure of PbTe along ⟨111⟩ direction. Band structure of PbTe (b) without and (c) with spin-orbit coupling.

on the physics of SnTe. For example, Tanaka *et al.* have performed ARPES measurements on PbTe (001) surfaces [23]. Yan *et al.* have taken ARPES spectra of $Pb_{1-x}Sn_xTe$ (111) thin films using a helium lamp [24]. Their results show that PbTe does not host evident topological protected gapless surface states and only states near band edge were observed. However, high-resolution band mapping of PbTe (111) over a large energy and momentum scale and the detailed comparison with theoretical calculation is still missing for the important (111) surface, the study of which may contribute to our understanding of the physics in these materials.

In this paper, using synchrotron-based high-resolution ARPES, we examine the electronic band dispersion of PbTe (111) thin films grown by MBE. The comparison between the experimental data and first-principles calculations helps us to identify the bulk and surface electronic band structures of PbTe (111) thin films.

II. METHODS

Molecular beam epitaxy. High-quality single-crystal thin films (∼1 μm) of PbTe were grown on freshly cleaved (111)-oriented BaF_2 substrates by MBE with a base pressure better than 2×10^{-10} Torr [10,25]. The substrates were prebaked for 30 min at 500 °C before the growth of PbTe films. 1-μm PbTe films were grown at a rate of 1 μm/h (a beam flux of 5×10^{-7} Torr) and the substrate temperature was kept at $T = 250$ °C. To keep equilibrium stoichiometry, an additional Te effusion cell was used during growth. The growth surface was monitored by reflection high-energy electron diffraction (RHEED). Because TeO_2 can easily form on the PbTe surface when the samples are exposed to air, a selenium capping layer about 200 nm was deposited on the top surface of PbTe films to protect them from oxidation during the transfer from the MBE chamber to the ARPES facility [26].

ARPES measurements. The ARPES experiments were carried out at beam line 13U of the National Synchrotron Radiation Laboratory (NSRL) at Hefei, China, using a Scienta R4000 electron spectrometer. Angle resolution was 0.3°, and the combined instrumental energy resolution was better than 20 meV. All samples were measured at 25 K under a vacuum better than 5×10^{-11} mbar. The Se cappling layer of PbTe samples was removed by sputtering for 10 min with 500-eV Ar^+ ions and annealed for 5 min at a temperature of 250 °C.

First-principles calculation. The electronic structures and total energy were calculated using first-principles density functional theory as implemented in the VASP package [27]. The projector-augmented-wave method was used with a plane-wave expansion up to 400 eV. The modified Becke and Johnson exchange potential (termed TB-mBJ) [28] was adopted to improve the description of bulk band structures. The TB-mBJ approach remarkably improved the local density approximation for the p-p–like band gap and the error of the band gap is expected to be small. Spin-orbit interaction was included in the self-consistent calculation following the approach of Kleinman and Bylander [29]. Γ-centered $8 \times 8 \times 8$ Monkhorst-Pack k mesh was used for the Brillouin zone integration for the bulk. For the slab calculation, we used the supercell slab geometry with symmetric slabs with either cation or anion at both surfaces to avoid the polar field for the (111) crystal direction. The thickness of the vacuum region separating periodically repeated slabs was more than 20 Å and was tested up to 40 Å. We tested the convergence of our results up to slab thicknesses of 95 atoms. Γ-centered $7 \times 7 \times 1$ k mesh was used and the atomic geometries allowed to relax until the Hellmann-Feynman forces became smaller than 10 meV/Å within the generalized gradient approximation [30].

III. RESULTS AND DISCUSSION

A. Crystal structure and Brillouin zone

The fcc Bravais lattice of rock-salt crystal structure PbTe consists of two atoms. A view along the [111] direction of the fcc lattice shows six-layer periodicity and polar surface nature, which consists of alternating cation and anion layers as shown in Fig. 1(a). No reconstruction was observed for the PbTe (111) surface, as illustrated in the RHEED patterns during MBE growth [Fig. 2(a)], which is consistent with previous results [31].

The direct band gap of PbTe is at a fourfold valley degenerate L point of the fcc BZ [32], as shown in Fig. 1(a). The surface Brillouin zone (SBZ) of PbTe is hexagonal. The band-edge states at four L points are projected to one $\bar{\Gamma}$ point and three $\bar{M}$ points in hexagonal SBZ, respectively [Fig. 1(a)]. The rock-salt crystal structure of PbTe can be

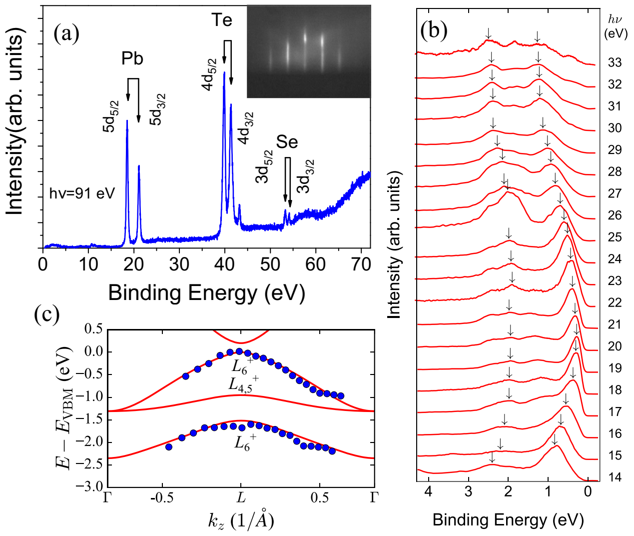

FIG. 2. (a) Angle-integrated PES of PbTe using 91.5-eV photons. The inset shows the RHEED pattern of a PbTe epitaxial film. (b) Photon-energy-dependent energy distribution curve (EDC) at normal emission where the arrows show the peaks in EDC. (c) The comparison of the measured peaks with the band dispersion obtained from first-principles calculation along Γ-L-Γ.

obtained by $\frac{1}{4}$ shift along the [111] direction of the cation and anion sublattices from the zinc-blende crystal structure. The additional inversion symmetry transforms the T_d point group of the zinc-blende structure to an O_h point-group symmetry of rock-salt structure and makes the energy bands at eight time-reversal-invariant momenta $(\Gamma, 4L, 3X)$ with definite parity, either positive parity or negative parity. The parity places a strong constraint for the band coupling. The calculations of the band structure for PbTe without and with spin-orbit coupling are plotted in Figs. 1(b) and 1(c). As shown in Fig. 1(c), the lone pair Pb 6s L_6^+ band couples strongly with the Te 5p valence electrons at the L point, pushing the L_6^+ valence band upwards, which makes the valence band maximum of PbTe at the L point. On the other hand, the Pb p orbital couples strongly with the high-lying conduction band with the same symmetry at the L point to make the L_6^- become the conduction band minimum. The coupling is stronger at low temperature due to the shorter bond length. Thus PbTe has a direct band gap of 0.32 eV at room temperature and 0.19 eV at 4 K at the L point (Table I).

B. The k_z measurement

The angle-integrated ultraviolet photoelectron spectroscopy measured with $h\nu = 91.5$-eV photons shows the core energy levels of Pb and Te [Fig. 2(a)], and the peak of Se is very weak after the Ar$^+$-ion bombardment. The inset in Fig. 2(a) is a RHEED image for the PbTe (111) growth surface by MBE. The streaky pattern indicates the smooth surface with a layer-by-layer growth process, which is critical for the following ARPES experiment. To gain the dispersion of the band structure along k_z, we measured photon-energy-dependent photoemission spectra from 14 eV to 45 eV with a step of 1 eV. The dispersion of the first and the third valence band of $L_6{}^+$ symmetry are clearly observed as shown in Fig. 2(b), proving their bulk origin. The top of valence band varies with the photon energy, and the maximum of valence band energy is found to be at 19 eV. The comparison between photoemission spectra and first-principles calculations along Γ-L-Γ is shown in Fig. 2(c), and the agreement between them is evident.

In the photoemission process, energy and momentum conservation holds. The momentum of photons is neglectful compared with the momentum of electrons in the spectral range adopted herein. Assuming an unreconstructed surface, the in-plane momentum of electrons is conserved and can be deduced by the relation $k_\parallel = \sqrt{2m_e E_{\mathrm{kin}}} \sin\theta/\hbar$, where E_{kin} is the measured kinetic energy of outgoing electrons and θ is the polar emission angle. However, the momentum component perpendicular to the surface is not conserved due to the break of translational symmetry by the surface. The strong dispersion with photon energy indicates that direct (dipole) transition plays an important role in the photoemission of PbTe (111) surfaces. By varying the photon energy we can probe different k_z values. Within the direct-transition model of the photoemission process, the dependence of k_z on photon energy can be modeled by assuming a free-electron final state [36]:

$$\frac{\hbar^2 k_z^2}{2m_e} - V_0 = E_{\mathrm{kin}} \cos^2\theta, \tag{1}$$

where V_0 is the inner potential. The valence band maximum at 19 eV is the L point in the second BZ [Fig. 2(b)]. The inner potential V_0 is estimated to be 5.9 eV, and the Γ point in the third BZ is fitted to be corresponding to $h\nu = 41$ eV.

C. The $k_\parallel$ measurement

Figure 3 shows the mapping along the $\bar{\Gamma}$-$\bar{K}$ cut. Only valence bands are accessible in all mappings, because unintentionally doped PbTe is typically of p-type conductivity due to Pb vacancies. The dispersion is quite different from the results of the (100) surface due to the different k-point sampling from the different crystal direction [18,20]. We find that the overall band dispersion agrees well between the ARPES experiment and the direct-transition model calculation in Figs. 3(a)–3(f).

TABLE I. Lattice constants, dielectric constants, effective masses, and energy-band gaps of PbTe.

			$E_g(L)$(eV)	
a (Å) (Ref. [14])	ε (Ref. [33])	m^*/m_e (Ref. [34])	Calc.	Expt. (Ref. [35])
6.428 (30 K)	$\varepsilon_0 = 414$	$m_\perp^e = 0.022, m_\parallel^e = 0.185$	0.20	0.19 (4 K)
6.462 (300 K)	$\varepsilon_\infty = 40$	$m_\perp^h = 0.025, m_\parallel^h = 0.236$		0.32 (300 K)

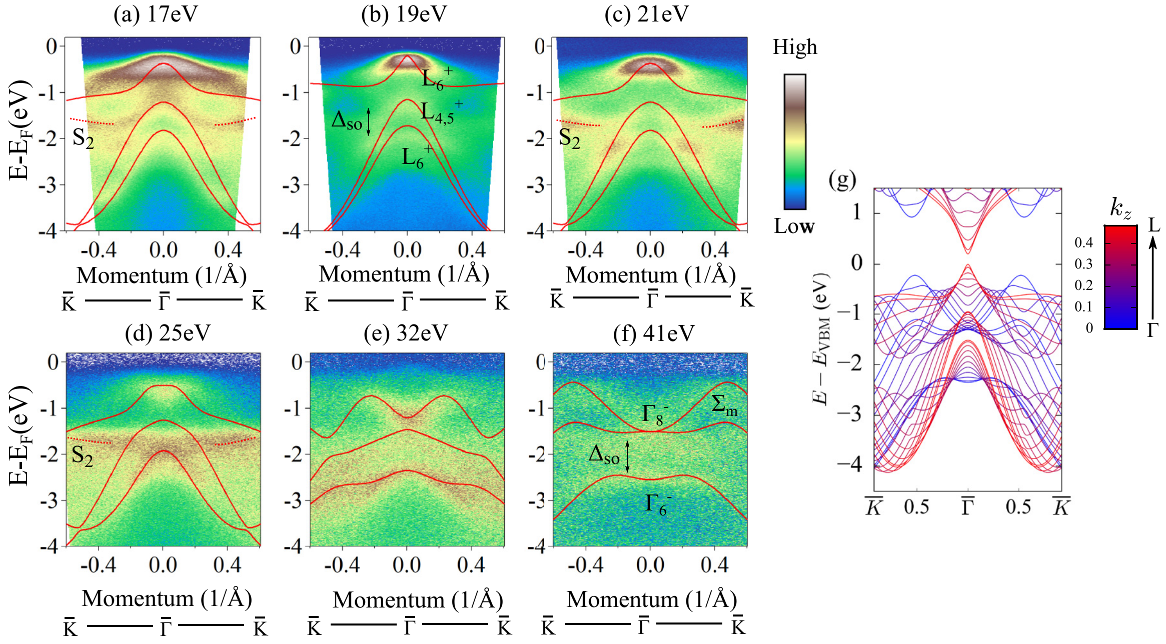

FIG. 3. (a)–(f) ARPES dispersions along $\bar{\Gamma}$-$\bar{K}$ of a PbTe (111) film taken by horizontal polarized photons with different energies. The lines overlaid are calculated energy-band dispersions. Surface states are labeled by dotted lines. (g) The calculated band structure of PbTe (111) projected onto the SBZ with different k_z values shown by the color of the lines.

Figure 3(g) shows the projected band structure of PbTe (111) with different k_z, i.e., the calculated band structure with a uniform interval of k_z within the first BZ. Different line colors in Fig. 3(g) indicate varied k_z values. The bulk band structure along the wave vector path Γ-L, denoted as k_z, is projected onto the path connecting $\bar{\Gamma}$ and $\bar{K}$ in the hexagonal SBZ. The resulting counts of energy levels in unit energy intervals at each k_z point shown in Fig. 3(g) are proportional to the density of states and should resemble the ARPES maps.

The band dispersions passing through the Σ_m point are shown in Fig. 3(f). The Σ-line valence band maximum (Σ_m) of PbTe is the second highest valence band. Σ_m is located near the midpoint of the Σ line in the fcc BZ [Fig. 1(a)] and has 12-fold degeneracy. The convergence of L and Σ_m is the key factor to the enhancement of thermoelectric figure of merit of PbTe-based alloy [8]. The energy difference between the L and Σ_m point has not been clearly determined in previous studies. By performing ARPES measurements on the (111) surface we can find one of the Σ_m points in the k_z plane across the Γ point along the $\bar{\Gamma}$-$\bar{K}$ cut. The energy difference between the L and Σ_m point is 0.2 eV.

The spin-orbit coupling plays an important role in PbTe energy bands as the component elements involved are heavy. The value of spin-orbit splitting varies at the L and Γ point, which arises from the different weights of atomic orbital mixing. At the L and Γ point shown in Figs. 3(b) and 3(f), the splitting between the second and third valence bands due to spin-orbit interaction is $\Delta_{\mathrm{SO}}(L) = E(L_{4,5}^+ - L_6^+) =$ 0.62 eV and $\Delta_{\mathrm{SO}}(\Gamma) = E(\Gamma_8^- - \Gamma_6^-) = 0.88$ eV, which agrees well with the calculated value of 0.57 eV and 1.05 eV, respectively. These values are approximately 3 times the 0.2 eV and 0.34 eV at the L and Γ point in GaAs, respectively [37].

We also note a feature at around 1.7 eV below the Fermi level in Figs. 3(a), 3(c), and 3(d) which does not disperse with photon energy. This feature, highlighted by dotted lines, cannot fit into the calculated bands by either the direct or the indirect-transition model. We assign this band to a surface state (or resonance, S_2). The S_2 band dominates the photoemission process at $h\nu = 25$ eV [Fig. 3(d)], whereas its intensity is much weaker than the direct-transition peaks from 14 eV to 23 eV. The intensity variation of S_2 in Fig. 3 as a function of photon energy can be attributed to a matrix element effect [38]. The theoretical calculation could help us to disentangle surface states from the bulk band structures. We further employed a symmetric slab composed of 59 atomic layers (~110 Å) with Te atoms at both ends of PbTe to simulate the surface states. In Fig. 4(a), the red dots show the bands with significant weight from surface Te atoms. The surface states are labeled S_1, S_2, and S_3. The calculated S_2 band should be shifted downward about 1.0 eV to match with the experimental data due to the usage of a semilocal functional, which usually has an error estimation of band gaps. Though the S_2 state is observed only away from the Γ point it could continue through the $\bar{\Gamma}$ point or overlap with the bulk bands, as seen in the calculated results of Fig. 4(a). The difficulty to distinguish the S_2 and $L_{4,5}^+$ states near the $\bar{\Gamma}$ point is due to their proximity in energy and similarity of band profiles.

We note that the hole effective mass discrepancy between the measured ARPES data and the calculated bands, i.e., the hole effective mass of the calculated bands, is obviously smaller than that measured by ARPES in the range from 17 eV to 21 eV [Figs. 3(a)–3(c)]. This issue could be explained by the surface states as well. We notice from the calculation result that there are surface states near the valance band edge (S_1), which explains the unexpected large effective mass of

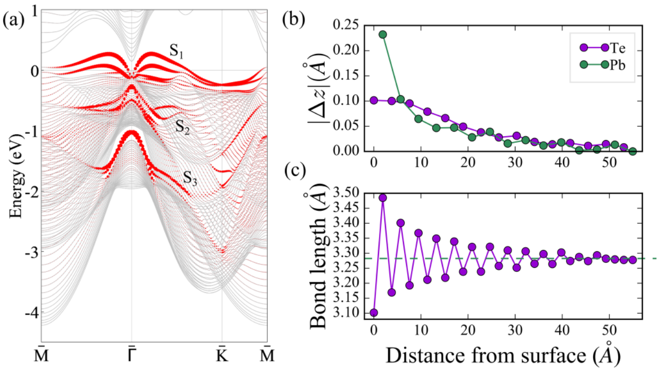

FIG. 4. (a) Calculated band structure using a semilocal functional of a PbTe symmetric slab. The size of the red dots marks the weight of the wave function projected to the spheres around the first two surface Te atoms. (b) The shift of atomic positions in z direction relative to the bulk positions. (c) The bond length as a function of distance from the surface. The positions of the bonds are defined as the positions of starting atoms, and the dashed line in (c) shows the bulk bond length.

the valence states. Such surface states are not unfamiliar, e.g., α-GeTe was recently known to show similar surface states [39]. The surface states near the band edge could influence transport and optical properties of PbTe. The effect of surface passivation of PbTe surface states in heterojunctions and nanostructures is not fully explored yet.

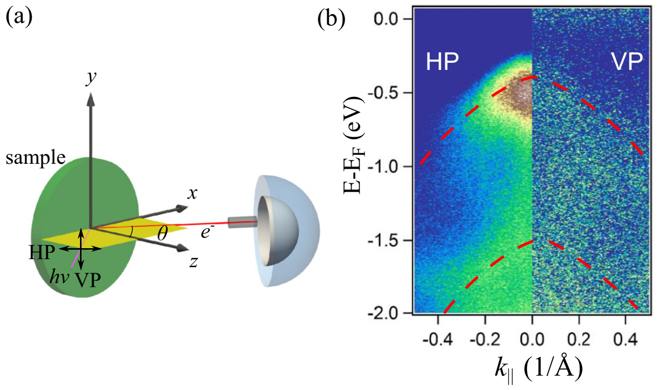

FIG. 5. (a) Geometry of the photoemission process. The PbTe sample and the plane defined by incident light and analyzer slit are shown by green and yellow colors, respectively. Horizontal and vertical linearly polarized light are marked. (b) APRES mapping along $\bar{\Gamma}$-$\bar{K}$ by excitation of HP and VP photons.

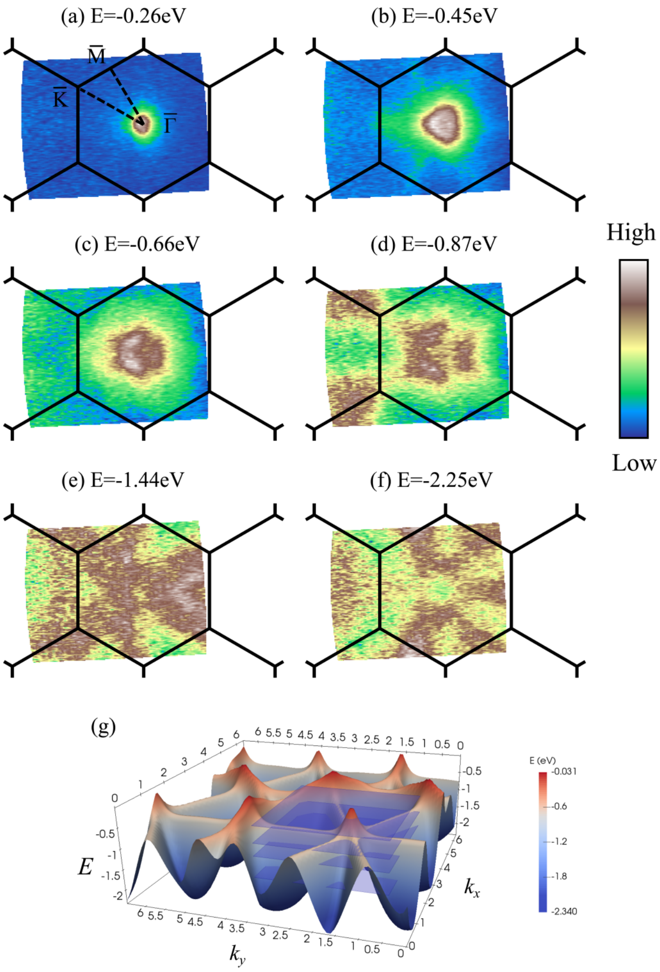
(a) E=-0.26eV
(b) E=-0.45eV
(c) E=-0.66eV
(d) E=-0.87eV
(e) E=-1.44eV
(f) E=-2.25eV
(g)

FIG. 6. (a)–(f) A stack of ARPES isoenergetic contours at different energies below the Fermi level. The black lines mark the Brillouin zone boundaries. (g) Calculated energy eigenvalues of the first valence band.

The orbital character can also be resolved when photons with various polarizations are used in ARPES [Fig. 5(a)]. Since the vector potential for vertical polarization (VP) lies in the in-plane $\bar{\Gamma}$-$\bar{K}$ direction, it only probes electronic states that do not possess even parity along this direction. The valence band arises from Te $5p_z$, and Pb $6s$ orbitals have approximately even parity along the $\bar{\Gamma}$-$\bar{K}$ direction; thus their intensity should be largely suppressed with VP photons. This is indeed observed experimentally in Fig. 5(b). On the other hand, since the vector potential for horizontal polarization (HP) has both in-plane and out-of-plane components, which allows photoexcitation from orbitals with different symmetries, valence bands show up clearly in this case. Our first-principles calculation confirms that the valence band of PbTe is mainly composed of Te $5p$ and Pb $6s$ orbitals in which Te $5p$ contributes 62% while Pb $6s$ has 36%. As PbTe has a cubic crystal structure, p_z, p_x, and p_y should have the same contribution (21%) to the valence band in a bulk crystal [22]. However, in ARPES data only the p_z component can be observed. This phenomenon could be due to the breakdown of the bulk cubic symmetry near the PbTe surface. We tested the idea by examining the slab calculation with relaxed atomic positions. The shift of cations and anions and the change of bond length relative to bulk ones were obtained [see Figs. 4(b) and 4(c)]. Specifically, the bond length varies between 3.10 Å and 3.48 Å and shows a dramatic change relative to the bulk bond length. The bond lengths are gradually restored to the bulk value about 20 Å from the surface. Based on the universal mean free path for photoelectrons in solids [36], the electron escape path is estimated to be less than 5 Å for the photon energy adopted in our experiment, corresponding to the first two or three layers in PbTe. Consequently, the surface effect is prominent in our photoemission experiment. The layered distortion near the surface stems from the structural instability of PbTe [33] and is very similar to another group-IV chalcogenide, SnSe, with a layer-distorted rock-salt structure, which recently shows a thermoelectric figure of merit of record high along the in-plane *b* axis of its layered structure [40,41]. Here, the distorted structure at the PbTe (111) surface could be a potential pathway to improve the thermoelectric figure of merit of PbTe.

We further examine the angular variation of the photoemission spectroscopy. Figure 6 shows the energy contours at several representative energies below the Fermi level. Close to the valence band maximum, the contours are quite isotropic with circular shape, but they become much more anisotropic as the energy decreases, reflecting the underlying bulk band nature as a result of crystal field. In particular, a snowflake shape of spectral weight is observed with six lobes along the $\bar{\Gamma}$-$\bar{M}$ symmetry line of the hexagonal SBZ between $E = -1.44$ eV and -2.25 eV, revealing the hexagonal symmetry of the rock-salt structure along [111] direction. These features are well captured in the band structure calculation shown in Fig. 6(g) in which the calculated eigenvalue of the top valence band is given. The hexagonal warping effect leads to a variety of interesting results, such as out-of-plane spin polarization for the Dirac cone of the topological insulator Bi_2Te_3 [42]. The observed six lobes along $\bar{\Gamma}$-$\bar{M}$ make a large contribution to the electron density of states near the valence band maximum, which is important for the outstanding thermoelectric performance of PbTe.

IV. CONCLUSIONS

The energy-band dispersions both perpendicular and parallel to the Γ-L direction were obtained by varying the incident photon energies and polarizations in ARPES measurements. The combination of ARPES and first-principles calculation clearly reveals the full 3D band structure, orbital characters, spin-orbit splitting energies, and surface states. The photon-energy-dependent spectra show the bulk character. Both the L and Σ valence bands are observed and their energy difference is determined to be 0.2 eV. The spin-orbit splitting energies at L and Γ points as large as 0.62 eV and 0.88 eV are identified, respectively. The surface states below and close to the valence band maximum are unambiguously identified. By varying the photon polarization, the valence bands are observed to be composed of a mixture of Pb $6s$ and Te $5p_z$ orbitals with mostly in-plane even parity, which is attributed to the layered distortion in the vicinity of the PbTe (111) surface. From the measured constant-energy contours, the valence bands show a transition from isotropic to anisotropic away from the L point as a result of crystal field. These findings are of importance not only for fundamental research but also for thermoelectric and optoelectronic device applications based on PbTe.

ACKNOWLEDGMENTS

This work was supported by the National Natural Science Foundation of China (Grants No. 61290305 and No. 11374259), Thousand Youth Talents Plans, and the National R&D Program of the MOST, China (Grant No. 2016YFA0300203).

---

[1] D. Khokhlov, *Lead Chalcogenides: Physics and Applications* (CRC Press, Boca Raton, FL, 2002).

[2] G. Springholz, Molecular beam epitaxy of IV–VI semiconductors: Multilayers, quantum dots and device applications, in *Molecular Beam Epitaxy: From Research to Mass Production*, edited by M. Henini (Elsevier, Oxford, 2013), pp. 263–310.

[3] J. P. Heremans, V. Jovovic, E. S. Toberer, A. Saramat, K. Kurosaki, A. Charoenphakdee, S. Yamanaka, and G. J. Snyder, Enhancement of thermoelectric efficiency in PbTe by distortion of the electronic density of states, Science **321**, 554 (2008).

[4] K. Biswas, J. He, I. D. Blum, C.-I. Wu, T. P. Hogan, D. N. Seidman, V. P. Dravid, and M. G. Kanatzidis, High-performance bulk thermoelectrics with all-scale hierarchical architectures, Nature (London) **489**, 414 (2012).

[5] H. Zogg, M. Rahim, A. Khiar, M. Fill, F. Felder, and N. Quack, Mid infrared resonant cavity detectors and lasers with epitaxial lead-chalcogenides, Opto-Electron. Rev. **18**, 231 (2010).

[6] A. Hochreiner, T. Schwarzl, M. Eibelhuber, W. Heiss, G. Springholz, V. Kolkovsky, G. Karczewski, and T. Wojtowicz, Midinfrared electroluminescence from PbTe/CdTe quantum dot light-emitting diodes, Appl. Phys. Lett. **98**, 021106 (2011).

[7] A. Khiar, V. Volobuev, M. Witzan, A. Hochreiner, M. Eibelhuber, and G. Springholz, In-well pumped mid-infrared PbTe/CdTe quantum well vertical external cavity surface emitting lasers, Appl. Phys. Lett. **104**, 231105 (2014).

[8] Y. Pei, X. Shi, A. LaLonde, H. Wang, L. Chen, and G. J. Snyder, Convergence of electronic bands for high performance bulk thermoelectrics, Nature (London) **473**, 66 (2011).

[9] T. H. Hsieh, H. Lin, J. Liu, W. Duan, A. Bansil, and L. Fu, Topological crystalline insulators in the SnTe material class, Nat. Commun. **3**, 982 (2012).

[10] B. Zhang, P. Lu, H. Liu, L. Jiao, Z. Ye, M. Jaime, F. F. Balakirev, H. Yuan, H. Wu, W. Pan, and Y. Zhang, Quantum oscillations in a two-dimensional electron gas at the rocksalt/zincblende interface of PbTe/CdTe (111) heterostructures, Nano Lett. **15**, 4381 (2015).

[11] D. L. Mitchell and R. F. Wallis, Theoretical energy-band parameters for the lead salts, Phys. Rev. **151**, 581 (1966).

[12] Y. W. Tung and M. L. Cohen, Relativistic band structure and electronic properties of SnTe, GeTe, and PbTe, Phys. Rev. **180**, 823 (1969).

[13] C. S. Lent, M. A. Bowen, J. D. Dow, R. S. Allgaier, O. F. Sankey, and E. S. Ho, Relativistic empirical tight-binding theory of the energy bands of GeTe, SnTe, PbTe, PbSe, PbS, and their alloys, Superlattices Microstruct. **2**, 491 (1986).

[14] K. Hummer, A. Grüneis, and G. Kresse, Structural and electronic properties of lead chalcogenides from first principles, Phys. Rev. B **75**, 195211 (2007).

[15] A. Svane, N. E. Christensen, M. Cardona, A. N. Chantis, M. van Schilfgaarde, and T. Kotani, Quasiparticle self-consistent

GW calculations for PbS, PbSe, and PbTe: Band structure and pressure coefficients, Phys. Rev. B **81**, 245120 (2010).

[16] M. Cardona and D. L. Greenaway, Optical properties and band structure of group IV-VI and group V materials, Phys. Rev. **133**, A1685 (1964).

[17] D. E. Aspnes and M. Cardona, Electro-optic measurements of PbS, PbSe, and PbTe, Phys. Rev. **173**, 714 (1968).

[18] T. Grandke, L. Ley, and M. Cardona, Angle-resolved UV photoemission and electronic band structures of the lead chalcogenides, Phys. Rev. B **18**, 3847 (1978).

[19] P. Y. Yu and M. Cardona, *Fundamentals of Semiconductors: Physics and Materials Properties* (Springer, New York, 2010).

[20] V. Hinkel, H. Haak, C. Mariani, L. Sorba, K. Horn, and N. E. Christensen, Investigation of the bulk band structure of IV-VI compound semiconductors: PbSe and PbTe, Phys. Rev. B **40**, 5549 (1989).

[21] L. Fu, Topological Crystalline Insulators, Phys. Rev. Lett. **106**, 106802 (2011).

[22] Z.-Y. Ye, H.-X. Deng, H.-Z. Wu, S.-S. Li, S.-H. Wei, and J.-W. Luo, The origin of electronic band structure anomaly in topological crystalline insulator group-IV tellurides, Npj Comput. Mater. **1**, 15001 (2015).

[23] Y. Tanaka, Z. Ren, T. Sato, K. Nakayama, S. Souma, T. Takahashi, K. Segawa, and Y. Ando, Experimental realization of a topological crystalline insulator in SnTe, Nat. Phys. **8**, 800 (2012).

[24] C. Yan, J. Liu, Y. Zang, J. Wang, Z. Wang, P. Wang, Z.-D. Zhang, L. Wang, X. Ma, S. Ji, K. He, L. Fu, W. Duan, Q.-K. Xue, and X. Chen, Experimental Observation of Dirac-Like Surface States and Topological Phase Transition in $\mathrm{Pb}_{1\text{-}x}\mathrm{Sn}_x\mathrm{Te}(111)$ Films, Phys. Rev. Lett. **112**, 186801 (2014).

[25] B. Zhang, C. Cai, S. Jin, Z. Ye, H. Wu, and Z. Qi, Resonant nature of intrinsic defect energy levels in PbTe revealed by infrared photoreflectance spectroscopy, Appl. Phys. Lett. **105**, 022109 (2014).

[26] H. Wu, C. Cao, J. Si, T. Xu, H. Zhang, H. Wu, J. Chen, W. Shen, and N. Dai, Observation of phonon modes in epitaxial PbTe films grown by molecular beam epitaxy, J. Appl. Phys. **101**, 103505 (2007).

[27] G. Kresse and D. Joubert, From ultrasoft pseudopotentials to the projector augmented-wave method, Phys. Rev. B **59**, 1758 (1999).

[28] F. Tran and P. Blaha, Accurate Band Gaps of Semiconductors and Insulators with a Semilocal Exchange-Correlation Potential, Phys. Rev. Lett. **102**, 226401 (2009).

[29] L. Kleinman and D. M. Bylander, Efficacious Form for Model Pseudopotentials, Phys. Rev. Lett. **48**, 1425 (1982).

[30] J. P. Perdew, K. Burke, and M. Ernzerhof, Generalized Gradient Approximation Made Simple, Phys. Rev. Lett. **77**, 3865 (1996).

[31] S. Jin, C. Cai, B. Zhang, H. Wu, G. Bi, J. Si, and Y. Zhang, Twisted ZB–CdTe/RS–PbTe (111) heterojunction as a metastable interface structure, New J. Phys. **14**, 113021 (2012).

[32] S.-H. Wei and A. Zunger, Electronic and structural anomalies in lead chalcogenides, Phys. Rev. B **55**, 13605 (1997).

[33] S. Jin, C. Cai, G. Bi, B. Zhang, H. Wu, and Y. Zhang, Two-dimensional electron gas at the metastable twisted interfaces of CdTe/PbTe (111) single heterojunctions, Phys. Rev. B **87**, 235315 (2013).

[34] H. Preier, Recent advances in lead-chalcogenide diode lasers, Appl. Phys. **20**, 189 (1979).

[35] T. N. Xu, H. Z. Wu, J. X. Si, and P. J. McCann, Optical transitions in PbTe/CdTe quantum dots, Phys. Rev. B **76**, 155328 (2007).

[36] S. Hüfner, *Photoelectron Spectroscopy: Principles and Applications* (Springer-Verlag, Berlin, 2003).

[37] J.-W. Luo, G. Bester, and A. Zunger, Full-Zone Spin Splitting for Electrons and Holes in Bulk GaAs and GaSb, Phys. Rev. Lett. **102**, 056405 (2009).

[38] J. Ren, L. Fu, G. Bian, M. Wong, T. Wang, G. Zha, W. Jie, T. Miller, M. Z. Hasan, and T. C. Chiang, Spectroscopic studies of CdTe(111) bulk and surface electronic structure, Phys. Rev. B **91**, 235303 (2015).

[39] J. Krempaský, H. Volfová, S. Muff, N. Pilet, G. Landolt, M. Radović, M. Shi, D. Kriegner, V. Holý, J. Braun, H. Ebert, F. Bisti, V. A. Rogalev, V. N. Strocov, G. Springholz, J. Minár, and J. H. Dil, Disentangling bulk and surface Rashba effects in ferroelectric α-GeTe, Phys. Rev. B **94**, 205111 (2016).

[40] L.-D. Zhao, S.-H. Lo, Y. Zhang, H. Sun, G. Tan, C. Uher, C. Wolverton, V. P. Dravid, and M. G. Kanatzidis, Ultralow thermal conductivity and high thermoelectric figure of merit in SnSe crystals, Nature (London) **508**, 373 (2014).

[41] L.-D. Zhao, G. Tan, S. Hao, J. He, Y. Pei, H. Chi, H. Wang, S. Gong, H. Xu, V. P. Dravid, C. Uher, G. J. Snyder, C. Wolverton, and M. G. Kanatzidis, Ultrahigh power factor and thermoelectric performance in hole-doped single-crystal SnSe, Science **351**, 141 (2016).

[42] M. Nomura, S. Souma, A. Takayama, T. Sato, T. Takahashi, K. Eto, K. Segawa, and Y. Ando, Relationship between Fermi surface warping and out-of-plane spin polarization in topological insulators: A view from spin- and angle-resolved photoemission, Phys. Rev. B **89**, 045134 (2014).